



Laser-based series interconnection of chalcopyrite und perovskite solar cells: Analysis of material modifications and implications for achieving small dead area widths

Christof Schultz^a, Markus Fenske^{a,b}, Janardan Dagar^b, Guillermo A. Farias Basulto^c, Andreas Zeiser^a, Andreas Bartelt^a, Cornelia Junghans^d, Rutger Schlatmann^{a,c}, Eva Unger^b, Bert Stegemann^{a,*}

^aHTW Berlin - University of Applied Sciences, School of Engineering – Energy and Information, Wilhelminenhofstr. 75a, D-12459 Berlin, Germany

^bHelmholtz-Zentrum Berlin für Materialien und Energie, Young Investigator Group Hybrid Materials Formation and Scaling, Kekuléstraße 5, D-12489 Berlin, Germany

^cHelmholtz-Zentrum Berlin für Materialien und Energie, Photovoltaics Competence Centre Berlin (PVcomB), Schwarzschildstr. 3, D-12489 Berlin, Germany

^dBecker & Hickl GmbH, Nunsdorfer Ring 7-9, D-12277 Berlin, Germany

ARTICLE INFO

Article history:

Available online 19 August 2021

Keywords:

Laser
Photoluminescence
Photovoltaics
Series Interconnection
Solar Module
Thin Film

ABSTRACT

Both nanosecond pulses and picosecond laser pulses are used for P2 patterning of chalcopyrite (Cu(In,Ga)Se₂, CIGSe) and metal halide perovskite solar cell absorber layers. For CIGSe, the range of the modified material visualized by photoluminescence imaging is significantly wider than the actual physical line-width, since energy input by the laser pulses leads to material modification in the vicinity of the scribed lines. This effect does not occur with the perovskite absorber layers, where there is no apparent influence on the edge regions. From numerical calculations of the temperature depth-profiles and the surface temperature distributions it is concluded that this effect is due to the significantly lower perovskite absorber layer thickness compared to CIGSe and the nevertheless significantly higher laser fluence required for perovskite ablation. The unaffected edge regions around the P2 line in the perovskite enabled a reduction of the dead area width in the fabrication of 3-segmented mini-modules, which could be significantly reduced from 430 to 230 μm, while increasing the aperture area power conversion efficiency and also the geometric fill factor, which could be increased up to 94.6%.

© 2021 Elsevier Ltd. All rights reserved.

Selection and peer-review under responsibility of the scientific committee of the 11th Solid State Surfaces and Interfaces conference. This is an open access article under the CC BY-NC-ND license (<http://creativecommons.org/licenses/by-nc-nd/4.0/>).

1. Introduction

A major challenge in the fabrication of thin-film photovoltaic (PV) modules, such as chalcopyrite (Cu(In,Ga)Se₂, CIGSe) or metal halide perovskite PV modules, is the development of suitable processes and technologies that enable the high efficiencies achieved with small solar cells on a laboratory scale to be transferred to modules of larger, industrially relevant sizes [1–4]. The increase in thin film PV module size requires patterning of the solar cell area into solar cell stripes, which are interconnected in series. To achieve such an electrical interconnection, the patterning steps alternate with layer deposition steps during fabrication. In this way, a so-called monolithic series connection is obtained, which

adds the voltages of the neighboring cells and limits the current and thus the electrical losses.

Patterning can be performed conventionally by mechanical scribing with a needle or via pulsed laser ablation using nanosecond (ns) or picosecond (ps) laser pulses [5]. The process of needle patterning is more difficult to control since the tension created with the needle in the material might result in inhomogeneous line widths and residues in the trench. In contrast, laser patterning is based on controlled energy input, so that in principle regular and clean scribe lines can be produced [5]. However, the usage of laser-based techniques for heat-sensitive materials, such as CIGSe and perovskites, is still challenging as it always involves energy input into the underlying layer as well as into the edge regions of the lines [5] and will be addressed in this work.

In Fig. 1, the layer structure of both investigated solar cell types, i.e., a CIGSe solar cell in substrate configuration (Fig. 1a) and a planar perovskite solar cell in n-i-p configuration (Fig. 1b), as well as

* Corresponding author.

E-mail address: bert.stegemann@htw-berlin.de (B. Stegemann).

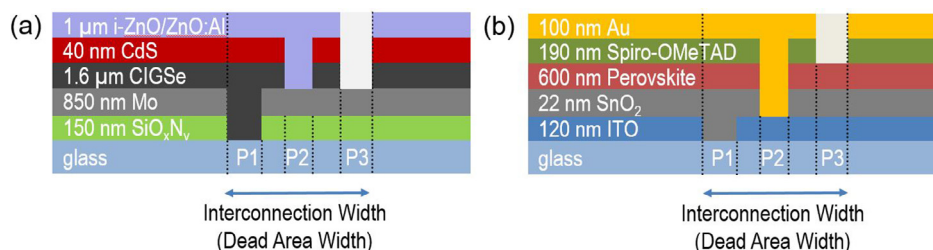


Fig. 1. Schematic representation of the layer stacks of (a) CIGSe and (b) perovskite solar cells. The respective materials and layer thicknesses are given. The principle of the monolithic series interconnection using three patterning steps (P1, P2, P3) is shown. Safety ranges are located between P1 and P2 as well as P2 and P3. The total sum of the line widths and the safety ranges determines the interconnection width (dead area width).

the three required patterning steps P1, P2 and P3 are schematically shown. The P1 and P3 lines separate the two contact layers and determine the width of the cells, which are thus electrically isolated from each other. The middle P2 structuring step provides the electrical interconnection between back to front contact by opening the absorber layer. Typically, the absorber layers are completely removed line-by-line, by ns or ps laser ablation, to produce a clean and smooth bottom of the patterned lines and thus to achieve low ohmic contact resistances [6]. However, a special feature of CIGSe is that, alternatively, the absorber layer can be converted with ns laser pulses into a highly conductive Cu-rich phase by selective evaporation of the absorber components to form the P2 interconnect [7,8].

As shown in Fig. 1, the distance between the outer edges of the P1 and P3 lines forms the interconnection area and, since it does not contribute to energy conversion, is also referred to as dead area width. In order to achieve a high cell-to-module efficiency ratio, this area must be kept as small as possible, which poses particular challenges to preserving the integrity of the edge regions of the absorber layer during P2 patterning. Lateral laser-induced material modifications in the absorber layer adjacent to the P2 scribe line can lead to lateral inhomogeneities and thus to non-optimal P3 patterning due to varying material properties, resulting in low shunt resistances and larger dead area zones.

2. Experimental section

2.1. Sample preparation

The CIGSe samples used for P2 patterning consist of the following layer stack (cf. Fig. 1a): Soda lime glass (SLG) substrate, 150 nm SiO_xN_y barrier layer, 850 nm Mo back contact including a thin layer of MoNa, 1.6 μm CIGSe absorber layer. The absorber layer was prepared by sequential deposition of Cu-In-Ga precursors, and subsequent annealing of the layer stack in N_2 atmosphere containing elemental Se at ambient pressure. All samples were etched in KCN and covered with a thin CdS buffer layer after patterning to avoid surface degradation [9].

For the P2 patterning of perovskite absorber layers, planar solar cell samples of the following layer sequence were prepared on a glass substrate (cf. Fig. 1b): 120 nm transparent indium-tin-oxide (ITO) front contact layer, 22 nm SnO_2 electron transport layer (ETL), 550–650 nm triple cation perovskite absorber layer ($\text{Cs}_{0.05}\text{FA}_{0.79}\text{MA}_{0.16}\text{PbBr}_{0.51}\text{I}_{2.49}$) prepared by spin-coating, 190 nm spiro-OMeTAD hole transport layer (HTL). For mini-module fabrication, a 100 nm Au gold back-contact layer completed the layer stack. Experimental details of the individual layer deposition parameters and processes are given elsewhere [10]. It should be added that the layer preparation is under continuous development. Variations in the composition of the solution

and thus also in the crystallization can lead to modified layer thicknesses.

Simulations of the heat propagation are performed to determine peak temperatures, temperature depth-profiles, and temperature distributions at the sample surface. Considerations for dead-area minimization are then derived from the extent and nature of the modified areas. Finally, first experimental implementations of perovskite mini-modules are demonstrated and evaluated, showing how reducing the distances of the P1 and P3 lines to P2 lines within the unaffected edge areas might increase the module efficiency as well as the geometric fill factor.

2.2. Laser patterning

For preparation of the P1-P3 scribe lines in the respective solar cell layers (cf. Fig. 1), a customized patterning tool (Rofin Baasel Lasertech) was used, which is equipped with high-precision linear motor drives for the x-y translation of the sample with up to 1.2 m/s. Two laser sources are available for patterning, a nanosecond laser and a picosecond laser. A detailed description of the lasers and the parameters can be found in Refs. [10,11]. The laser beam possesses a Gaussian intensity distribution. The corresponding beam diameters ($2\omega_0$) were determined at the sample surface by Liu's method [12]. The determination of suitable P2 and P3 patterning parameters, i.e. laser fluence F and pulse-to-pulse overlap OL , was the subject of previous work and was accomplished by preparing parallel lines with varying fluence. These lines were evaluated in terms of morphology, electrical functionality as well as reliability and stability of the process against slight preparation-related variations in material composition and film thickness [10,11,13,14]. The basic laser parameters as well as suitable parameters used for the successful P2 patterning are summarized in Table 1.

2.3. Characterization

The scribed lines and their vicinities were characterized by confocal optical microscopy (OM) and photoluminescence (PL) microscopy (Keyence VK-X250K PL, Becker & Hickl DCS-120). Current density–voltage (j-V) measurements were performed using a class AAA Wavelabs Sinus-70 sun simulator which was calibrated with a Si reference solar cell.

2.4. Numerical analysis

To explain the experimental observations, a model for the calculation of the heat propagation was developed, which takes into account the different layers and their material properties and thus allows a calculation of the peak temperatures, the temperature depth profile and the temperature distribution on the sample surface. In brief, the calculation is based on the heat conduction equa-

Table 1
Laser and patterning parameters.

Parameter	Symbol	Unit	CIGSe		Perovskite	
			ns laser	ps laser	ns laser	ps laser
Wavelength	λ	nm	532	532	532	532
Pulse duration	τ_p	s	30×10^9	10×10^{12}	20×10^9	10×10^{12}
Beam diameter	$2\omega_0$	μm	75	53	28	27
Fluence	F	J/cm^2	0.19	0.29	3.22	1.16
Overlap	OL	%	98	98	63	61

tion and the 1-temperature model, which assumes identical temperatures for the electrons and the lattice [15,16]. As boundary conditions it was assumed that there is no heat flow from the surface, such as convection, that the substrate is kept at constant temperature and plasma shielding can be neglected. A more comprehensive description of the theoretical approach can be found in Ref. [10].

3. Results and discussion

3.1. Experimental analysis of the P2 scribe line widths

The aim of the P2 laser patterning of the CIGSe and perovskite absorber layers is to create narrow laser trenches ($\approx 60 \mu\text{m}$) that ensure good electrical behavior of the monolithic interconnection. This was achieved with the laser fluences and pulse-to-pulse overlaps given in Table 1. These values were determined and optimized individually in earlier studies [10,14,17]. They each are in a range of suitable values that allow patterning yielding the best possible morphologies and also low-loss electrical interconnections.

Fig. 2 provides typical images of P2 scribe lines for ns and ps laser patterning of CIGSe absorber layers, each shown at the same magnification for direct comparison of the trench widths.

According to the OM images, both the application of ns and ps laser leads to similar results. Both lines have similar widths of $\approx 55 \mu\text{m}$ and $\approx 58 \mu\text{m}$, respectively. The scribe line obtained by ns laser pulses shows solidified Cu-rich material within the trench and distinct solidified regions adjacent to the scribe line, which is a characteristic feature of ns laser patterning [11,14]. Also in ps patterning, thermally affected zones adjacent to the scribe line are clearly visible despite the shorter pulse duration. The corresponding PL intensity images show in both cases a significantly larger scribe width of $\approx 75 \mu\text{m}$, indicating the extinction of the PL signal even outside of the physically scribed lines. The decrease in radiative recombination in these areas is a clear indication of an increase in non-radiative recombination processes due to increased defect state densities caused by laser-induced material modifications and decomposition.

A similar investigation comparing the line widths for ns and ps laser patterning was carried out on perovskite absorber layers, see Fig. 3. Here, too, it is possible to produce high-quality trenches of constant line widths with both pulse durations. The trenches are slightly wider when ps pulses are used, even though the line widths of the lasers are the same. However, there are little differences between the OM and PL recordings and the line widths almost match. In relation to the laser beam diameter, the pattern-

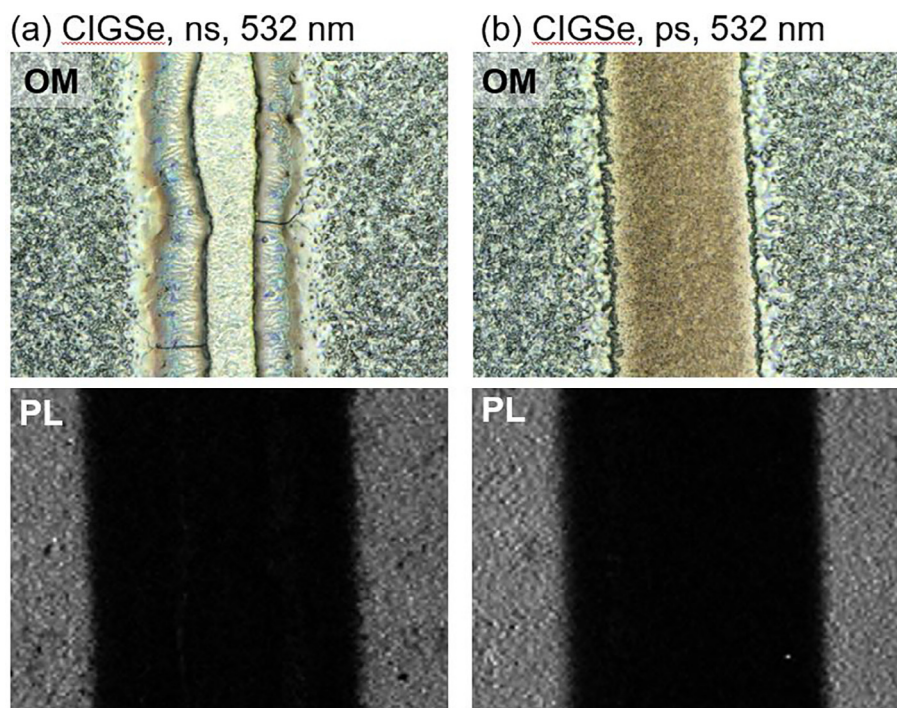


Fig. 2. Optical microscopy (OM) and photoluminescence (PL) intensity images of P2 scribe lines in CIGSe absorber layers: (a) ns laser pulses, (b) ps laser pulses. Width of all images: $120 \mu\text{m}$.

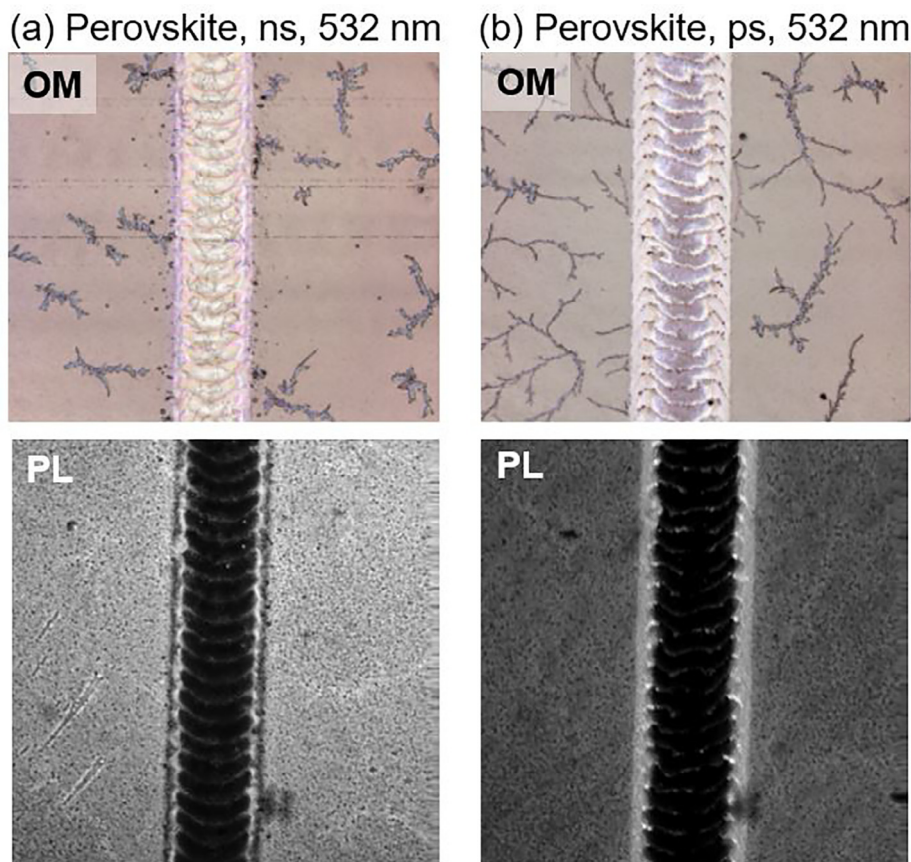


Fig. 3. Optical microscopy (OM) and photoluminescence (PL) intensity images of P2 scribe lines in perovskite absorber layers: (a) ns laser pulses, (b) ps laser pulses. Width of all images: 300 μm.

ing lines are significantly wider than in the CIGSe layers, but despite inherently high thermal sensitivity of the perovskite, no clearly visible thermally influenced edge regions appear here.

It can be stated that it is possible to produce P2 lines in both CIGSe and perovskite layers with both ns and ps laser pulses. The width of these lines agrees well and is in the range of about 55–65 μm in the examples shown. However, there are differences in the diameter of the laser beams used and in the modification of

the vicinity of the scribed lines. A quantitative analysis of the relationship between these quantities is shown in Fig. 4, which shows (i) the differences between the laser beam diameter and the physical linewidths determined by OM and (ii) the differences between the physical line widths (by OM) and the laser-affected line widths determined by PL. These results can be summarized as follows: For both materials, the width of the ablated lines differs from the diameter of the laser beam on the layer surface. In the case of perovskite, the line is significantly wider than the diameter of the laser beam. One explanation for the wide scribes in the perovskite layer is that, due to the significantly lower layer thickness (≈650 nm) and the differences in the thermal conductivities between the absorber and the ITO front contact layers, heat tends to accumulate at the perovskite-ITO interface and is reflected back into the material. In addition, since higher laser fluences are used for the perovskite layers, a relatively larger amount of material is removed and the scribe line edges are very steep. For the significantly thicker CIGSe layer (1.6 μm), there are similar thermal conductivities of the absorber and the metallic back contact and thus an almost continuous heat flow through the interface. The effect of heat accumulation is thus hardly pronounced and depends only on the length of the laser pulses. However, in the case of perovskite, no apparent damage or modification of the material occurs in the areas immediately adjacent to the patterned lines, even when the longer ns laser pulses are used and thus a comparatively high input of thermal energy occurs. The observations could also have their origin in the different layer thicknesses of the absorber (cf. Fig. 1) and the corresponding, larger laser fluences required for perovskite patterning, which will now be investigated by calculating the laser-induced heat flows.

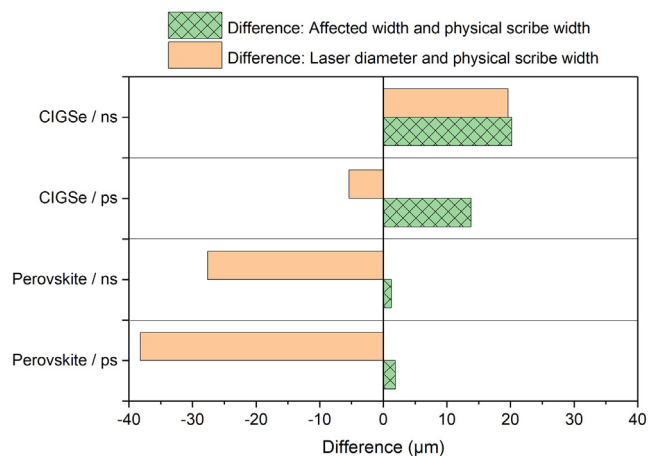


Fig. 4. Analysis of the P2 line widths in the OM and PL images for ns and ps patterning of CIGSe and perovskite layers (cf. Figs. 2 and 3). The graph shows the differences between the laser beam diameter and the physical linewidths determined by OM and the differences between the physical line widths (by OM) and the laser-affected line widths determined by PL.

3.2. Numerical analysis of the laser-induced heat flow

In order to understand the experimentally obtained results, the laser-induced heat flows in the direction of incidence through the materials were calculated by solving the 1-dimensional heat equation using MATLAB[®] and are shown in Fig. 5. These curves were reconstructed from the highest temperatures reached for each depth. In the case of CIGSe (see Fig. 5a), the temperature profiles refer to the 1.6 μm thick absorber layer processed with ns laser ($F = 0.19 \text{ J/cm}^2$) and ps laser ($F = 0.29 \text{ J/cm}^2$) pulses. It can be seen that the surface temperature exceeds (ps) or nearly reaches (ns) the melting temperature of CIGSe. Moreover, the calculated temperatures indicate selective evaporation of the absorber components, which agrees well with the previously observed experimental results of generating a Cu-rich phase by laser treatment of CIGSe [14]. The temperature decreases with increasing distance from the surface. The calculated temperature profiles give maximum temperatures at the CIGSe-Mo interface of about 560 K (ns) and 700 K (ps), respectively.

Corresponding calculations were performed for ns and ps laser patterning of the of the significantly thinner perovskite absorber layer. The fluences used for the calculations correspond to the values used for the patterning (see Fig. 3) and are 3.22 J/cm^2 for ns patterning and 1.16 J/cm^2 for ps patterning, respectively. This means that the fluence for ns patterning is higher than for the ps patterning, and that both fluences are also significantly higher than for CIGSe structuring. This ratio of the fluences is reflected in the behavior of the depth-dependent temperature profiles. The results in Fig. 5b show that the highest temperatures, which are found immediately after illumination of the sample surface, reach values of $4\text{--}5 \times 10^4 \text{ K}$. This means that the melting temperature of the perovskite of 633 K is exceeded by a factor of ≈ 70 . With regard to possible damage to the ITO front contact due to thermal influences, it is evident that temperatures are reached at the interface between the absorber and the front contact layers which, in the case of ns laser pulses, exceed the melting temperature of the

ITO front contact. It is known that this is accompanied by a decrease in the conductivity of the layer, i.e. thermally induced damage occurs [18]. The use of ps laser pulses causes significantly lower temperatures at that interface.

In addition, it should be mentioned that the heating rates in the irradiated volume, and thus the occurring ablation mechanisms can be derived from this temperature curves. The heating rates are above $1 \times 10^{12} \text{ K/s}$. The material is therefore strongly overheated, so that it abruptly begins to boil and evaporate throughout the irradiated volume. The resulting change in volume leads to explosive material ejection and ablation. A detailed discussion of the ablation mechanism can be found in Ref. [10].

3.3. Calculation of the surface temperature distribution

The processes discussed so far essentially explain the material removal. Conclusions about possible damages caused by the laser in the vicinity of the scribed lines are now to be derived from these calculations. In order to obtain the temperature profile on the surface across the scribed line, the Gaussian laser intensity distribution was transformed into a corresponding temperature distribution by calculating the fluences as a function of laser intensity. From these fluences, the laser-induced heat was calculated. Subsequently, the calculated peak temperatures are used to recursively generate the Gaussian temperature distribution at the sample surface.

The calculated temperature profile at the CIGSe surface, shown in Fig. 6a, indicates a peak temperature of about 1200 K in the center of the trench (cf. also Fig. 5a) and temperatures at the edges of the scribed line of about 1000 K. In the vicinity of the scribed line, the temperature decreases and reaches a value of 420 K at the outer edges of the laser affected areas. The thermal decomposition of CIGSe is known to start at temperatures of about 770 K [19] due to onset of Se^+ outgassing. Thus, the laser-induced material modifications in the edge regions can be attributed to the selective evaporation of the absorber components. While the PL images

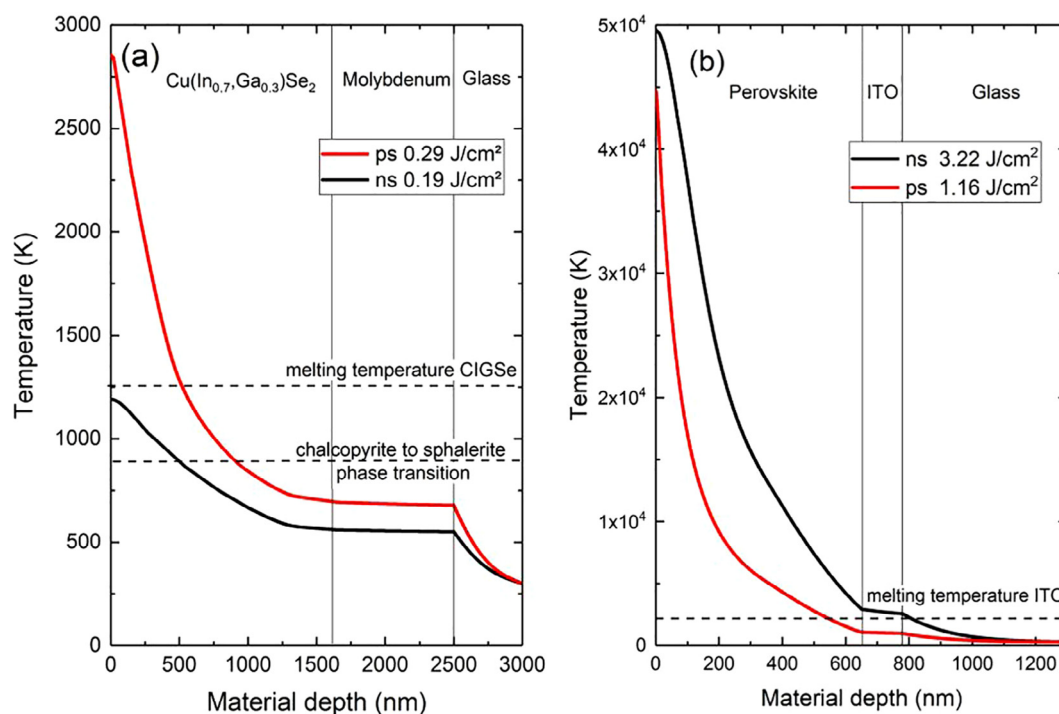


Fig. 5. Temperature profiles over the distance from the sample surface for ns and ps laser patterning of (a) CIGSe and (b) perovskite solar cell samples. The dashed horizontal lines indicate temperatures that are characteristic of the respective material modifications.

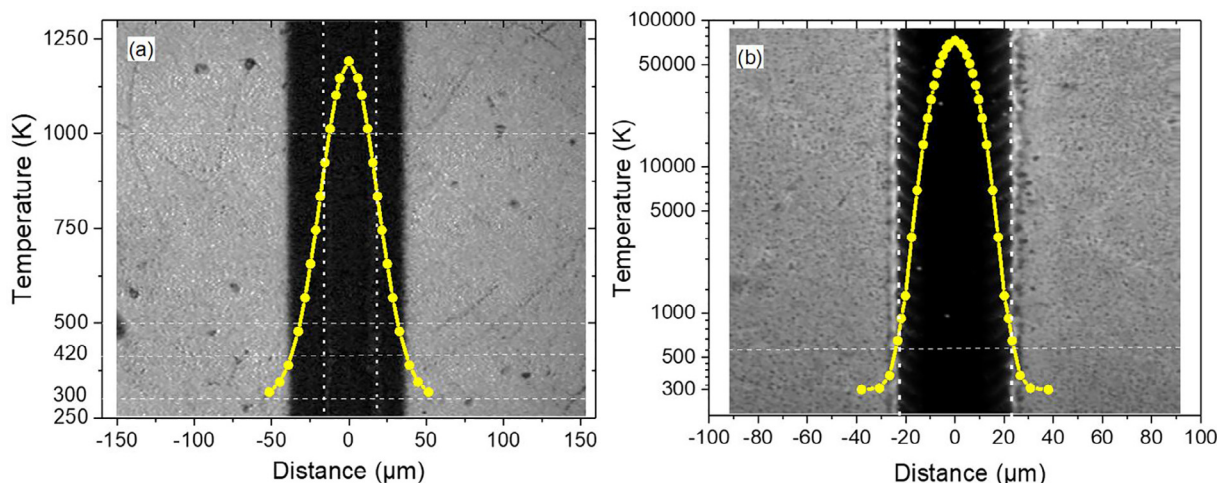


Fig. 6. Calculated Gaussian temperature profiles on the sample surface which are superimposed on PL intensity images of ns laser-patterned lines in (a) CIGSe ($F = 0.19 \text{ J/cm}^2$) and (b) perovskite ($F = 4.3 \text{ J/cm}^2$) layers. The width of the trenches is marked with vertical lines.

(Fig. 2) showed material modification at least $20 \mu\text{m}$ wider than the actual scribing line (cf. Fig. 3), previous investigations using spectrally and time-resolved PL showed that further material modification can occur at distances even up to $100 \mu\text{m}$ away from the line [11,14].

Similarly, the temperature profile on the perovskite sample surface was calculated using ns laser pulses for processing with ns laser pulses and is shown in Fig. 6b. The calculation was based on a slightly higher laser fluence (i.e., 4.3 J/cm^2) than the one used previously (3.22 J/cm^2). This value is at the upper end of the suitable laser fluence range for P2 structuring [10]. The calculated temperatures can thus be regarded as an upper limit estimate.

The profile of the perovskite surface temperature calculated in this way is logarithmically scaled due to the high peak temperature and superimposed with the corresponding PL intensity image of the scribed line. The horizontal line marks the position where the temperature curve intersects the edges of the scribed trench (marked by vertical lines). The high peak temperature of about $72,000 \text{ K}$ decreases rapidly and at the scribe line edges a temperature of about 600 K is obtained. This value is close to the melting point of Pb. It is concluded that the perovskite decomposes by sublimation of the organic moiety (sublimation temperature of $\text{CH}_3\text{-NH}_3$: 520 K [20]) and subsequent evaporation of the remaining Pb and I. The scribe line edges remain free of laser-affected zones. Neither morphological changes nor increased electronic defect densities occur. This seems surprising, but it may be not only related to the determined behaviour of the heat propagation but also due the passivation of electronic defects at voids, grain boundaries and defects by PbI_2 [21], which can be formed during the laser-induced degradation of perovskite, as well as to self-healing effects in the perovskite [22].

3.4. Implications for achieving small dead area widths

The areas affected by the P2 patterning step should not extend into the electrically active areas of the cells that are interconnected in series. The total width of the laser-affected areas comprising both sides of the P2 scribe therefore determines the minimum interconnection width. Knowing the width of the affected area is therefore important for the proper positioning of the P2 line (in relation to P1) and the subsequent P3 line. Ideally, all three lines P1, P2 and P3 could be placed right next to each other. The P3 can even be placed with an overlap of 50% to the P2, which enables a further reduction of the dead area width. That this is practically

feasible has already been shown on silicon thin-film PV modules [23]. Currently it is also being elaborated on perovskite PV modules [24].

Knowing the width of the area affected in P2 patterning and consequently placing the P1 and P3 line at the respective outer edges of the affected P2 area, total interconnection widths of $250 \mu\text{m}$ at best are reasonably possible with CIGSe. However, due to the unaffected edge areas, perovskite solar cells offer attractive potential for significantly reducing the dead area width. To evaluate this potential, two perovskite mini-modules with different interconnection width were produced. For both P2 and P3 patterning, ps laser pulses were used. A detailed investigation on the determination of the suitable laser fluences for the P3 step can be found in Ref. [13]. For the first mini-module, the usual interconnection geometry with a P1/P2 distance of $165 \mu\text{m}$ and P2/P3 distance of $130 \mu\text{m}$ was chosen, resulting in a dead area width of $430 \mu\text{m}$. This value corresponds approximately to the current state of the art [25,26]. For the second perovskite mini-module, the distances were significantly reduced: P1/P2 to $60 \mu\text{m}$ and P2/P3 to $35 \mu\text{m}$, resulting in a dead area width of $230 \mu\text{m}$. Since the dead area width is reduced, the active area changes, which means that the layout must be adapted. By means of simulations, the optimum cell widths were determined to be 5 mm for dead area widths of $430 \mu\text{m}$ and 4 mm for dead area widths of $230 \mu\text{m}$. The corresponding geometric fill factors (GFFs), which are defined as the ratio of the active area in the module to the aperture ratio (sum of active area and dead area), are 92.1% and 94.6%, respectively.

The laser scanning microscopy images in Fig. 7a and 7b show the interconnection regions of the mini-modules with both dead area widths produced by means of complete laser patterning. The individual widths of the scribe lines P1, P2, and P3, as well as the interline spacing are marked in these images. The electrical functionality of these two mini-modules is verified by current-density/voltage (j-V) measurements. The corresponding j-V curves as well as the relevant electrical and geometric parameters are shown in Fig. 7c. The successful series connection of the three cells can be recognized by the tripling of the open-circuit voltage of the individual cells to over 3 V . The analysis of the corresponding j-V parameters shows, that the higher fill factor and the higher power conversion efficiency, which refers to the aperture area, are achieved from the mini-module with the smaller dead area. This higher efficiency can be explained by the increase of the GFF with constant active area and with decreased dead area, which in turn raises the efficiency. Furthermore, the slightly decreasing series

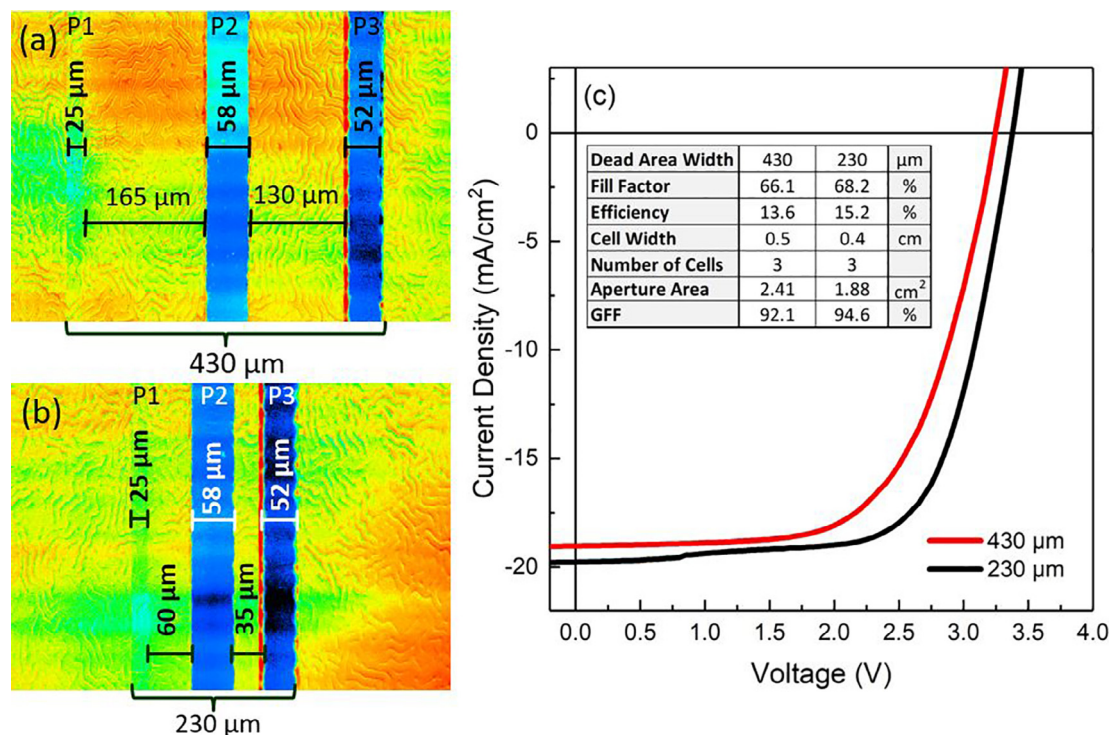


Fig. 7. Microscopy images of the interconnection regions with total widths of (a) 430 μm and (b) 230 μm . The P1–P3 scribe line widths and the widths of the line gaps (safety width) are indicated in the images. (c) Current-density voltage curves of the corresponding 3-segmented mini-modules. The electric and geometrical parameters are given in the inserted table.

resistance with smaller dead areas also has an efficiency-increasing effect.

4. Summary and conclusions

The laser-based series interconnection of CIGSe and perovskite solar cells was investigated with the aim of analyzing material modifications, especially in the vicinities of the respective P2 patterning lines, and deriving implications for minimizing the dead zone widths in the production of series-interconnected mini-modules. It was shown that both ns pulses and ps laser pulses can be used to pattern regular trenches with homogeneous linewidths in the range of 50–65 μm in both CIGSe and perovskite absorber layers. For P2 patterning of the CIGSe absorber layers, the results show a clear discrepancy between the physical linewidth visible by optical microscopy and the apparent width of the modified material visualized by PL imaging. The energy input by the laser pulses leads to material modification on the edge areas, which results in the formation of electronic defects and thus in the extinction of the PL signal. According to previous investigations using spectral and time-resolved PL these material modifications can even extend beyond the range visualized here, up to about 100 μm away from the scribe line [11]. This effect does not occur with the perovskite absorber layers. The P2 line width detected by PL, which is determined by the laser-induced impact, nearly matches the physical widths of the P2 lines (observed by OM), so that there is no apparent influence on the edge regions here.

By numerical analysis of the temperature propagation, temperature-depth profiles as well as the surface temperature distributions were calculated for the individual patterning variants. From these results, it can be concluded that the effect of the differ-

ent modifications of the scribe line edge regions is decisively related to the different absorber layer thicknesses (i.e. CIGSe: 1.6 μm , perovskite: 600 nm) in combination with its thermal properties (such as heat capacity and conductivity) and thus to the different laser fluences required for the patterning.

These results have a direct impact on the design of the interconnection area. While with CIGSe it is not helpful to place the P1 and P3 lines within the damaged area, which severely limits the possibility of minimizing the dead area, perovskite offers attractive possibilities to do so. This has also been successfully achieved by reducing the total interconnection width from 430 μm to 230 μm through smaller line gaps in 3-segmented perovskite mini-modules. By adjusting the cell stripe width with reduced dead area width, higher PCEs and GFFs were achieved with the module of smaller dead area.

It is worth mentioning that there is potential for further improvement, since interconnection widths of significantly less than 200 μm are feasible if the P1–P2 spacing is further reduced and the P2 line overlaps with the P3 line. This requires further process optimization and is subject of ongoing experiments.

CRedit authorship contribution statement

Christof Schultz: Investigation, Data curation, Visualization, Writing - review & editing. **Markus Fenske:** Investigation, Data curation. **Janardan Dagar:** Investigation, Methodology. **Guillermo A. Farias Basulto:** Investigation, Methodology, Visualization. **Andreas Zeiser:** Software. **Andreas Bartelt:** Investigation, Validation. **Cornelia Junghans:** Methodology, Investigation. **Rutger Schlatmann:** Resources, Supervision. **Eva Unger:** Methodology, Resources, Supervision. **Bert Stegemann:** Conceptualization, Visualization, Writing - original draft, Writing - review & editing, Supervision.

Declaration of Competing Interest

The authors declare that they have no known competing financial interests or personal relationships that could have appeared to influence the work reported in this paper.

Acknowledgements

The authors acknowledge the support of the PVcomB and the HZB (EE-IS) team, especially S. Schmidt and C.A. Kaufmann for experimental support. Moreover, the authors thank Jörn Bonse, Federal German Institute for Materials Research and Testing (BAM), for fruitful discussions. JD and EU acknowledge funding from the German Ministry of Education and Research (BMBF) for the Young Investigator Group Hybrid Materials Formation and Scaling (HyPerFORME) within the program “NanoMatFutur” (grant no. 03XP0091) and the “SNaPSHoTs” project (grant no. 011O1806).

References

- [1] N.-G. Park, K. Zhu, *Nat. Rev. Mater.* 5 (2020) 333.
- [2] G. Regmi, A. Adhikari, P. Chawla, P. Semalti, S. Sharma, H. Castaneda, *J. Mater. Sci.: Mater. Electron.* 31 (2020).
- [3] B. Kim, B.K. Min, *Sustainable Energy Fuels* 2 (2018) 1671.
- [4] L. Qiu, S. He, L.K. Ono, S. Liu, Y. Qi, *ACS Energy Lett.* 4 (2019) 2147.
- [5] B. Stegemann, C. Schultz, *Laser Patterning of Thin Films*, digital Encyclopedia of Applied Physics, 2019, Wiley VCH Verlag GmbH & Co. KGaA, pp. 1 – 30. <https://doi.org/10.1002/3527600434.eap830>.
- [6] P. Gečys, G. Račiukaitis, M. Ehrhardt, K. Zimmer, M. Gedvilas, *Appl. Phys. A* 101 (2010) 373.
- [7] C. Schultz, M. Schuele, K. Stelmaszczyk, M. Weizman, O. Gref, F. Friedrich, C. Wolf, N. Papathanasiou, C. Kaufmann, B. Rau, *Sol. Energy Mater. Sol. Cells* 157 (2016) 636.
- [8] P.O. Westin, U. Zimmermann, M. Ruth, M. Edoff, *Sol. Energy Mater. Sol. Cells* 95 (2011) 1062.
- [9] S.S. Schmidt, C. Wolf, H. Rodriguez-Alvarez, J.-P. Bäcker, C.A. Kaufmann, S. Merdes, F. Ziem, M. Hartig, S. Cinque, I. Dorbandt, C. Köble, D. Abou-Ras, R. Mainz, R. Schlatmann, *Prog. Photovoltaics Res. Appl.* 25 (2017) 341.
- [10] C. Schultz, M. Fenske, J. Dagar, A. Zeiser, A. Bartelt, R. Schlatmann, E. Unger, B. Stegemann, *Sol. Energy* 198 (2020) 410.
- [11] C. Schultz, A. Bartelt, C. Junghans, W. Becker, R. Schlatmann, B. Stegemann, *Appl. Surf. Sci.* 536 (2021) 147721.
- [12] J.M. Liu, *Opt. Lett.* 7 (1982) 196.
- [13] M. Fenske, C. Schultz, J. Dagar, F.U. Kosasih, A. Zeiser, C. Junghans, A. Bartelt, C. Ducati, R. Schlatmann, E. Unger, B. Stegemann, *Energy Technology* 9 (4) (2021) 2000969.
- [14] C. Schultz, G.A.F. Basulto, S. Ring, C. Wolf, R. Schlatmann, B. Stegemann, *IEEE J. Photovoltaics* 7 (2017) 1442.
- [15] J. Bovatsek, A. Tamhankar, R. Patel, N. Bulgakova, J. Bonse, *Thin Solid Films* 518 (2010) 2897.
- [16] A.V. Bulgakov, N.M. Bulgakova, *Quantum Electron.* 29 (1999) 433.
- [17] C. Schultz, F. Schneider, A. Neubauer, A. Bartelt, M. Jošt, B. Rech, R. Schlatmann, S. Albrecht, B. Stegemann, *IEEE J. Photovoltaics* 8 (2018) 1244.
- [18] D.-S. Liu, C.-S. Sheu, C.-T. Lee, C.-H. Lin, *Thin Solid Films* 516 (2008) 3196.
- [19] M. Ruckh, J. Kessler, T.A. Oberacker, H.W. Schock, *Jpn. J. Appl. Phys.* 32 (1993) 65.
- [20] A.E. Williams, P.J. Holliman, M.J. Carnie, M.L. Davies, D.A. Worsley, T.M. Watson, *J. Mater. Chem. A* 2 (2014) 19338.
- [21] B. Roose, K. Dey, Y.-H. Chiang, R.H. Friend, S.D. Stranks, *J. Phys. Chem. Lett.* 11 (2020) 6505.
- [22] Y. Rakita, I. Lubomirsky, D. Cahen, *Mater. Horiz.* 6 (2019) 1297.
- [23] B. Stannowski, O. Gabriel, S. Calnan, T. Frijnts, A. Heidelberg, S. Neubert, S. Kirner, S. Ring, M. Zelt, B. Rau, J.H. Zollondz, H. Bloess, R. Schlatmann, B. Rech, *Sol. Energy Mater. Sol. Cells* 119 (2013) 196.
- [24] M. Fenske, C. Schultz, J. Dagar, A. Bartelt, R. Schlatmann, E. Unger, B. Stegemann, submitted to Proc. 38th European Photovoltaic Solar Energy Conference and Exhibition, 2021.
- [25] F. Di Giacomo, L.A. Castriotta, F.U. Kosasih, D. Di Girolamo, C. Ducati, A. Di Carlo, *Micromachines* 11 (2020) 1127.
- [26] A.L. Palma, F. Matteocci, A. Agresti, S. Pescetelli, E. Calabrò, L. Vesce, S. Christiansen, M. Schmidt, A. Di Carlo, *IEEE J. Photovoltaics* 7 (2017) 1674.